




Miniaturized optical frequency reference for next-generation portable optical clocks

VINCENT MAURICE,^{1,3} ZACHARY L. NEWMAN,^{1,3,*} SUSANNAH DICKERSON,² MORGAN RIVERS,² JAMES HSIAO,² PHILLIP GREENE,² MARK MESCHER,² JOHN KITCHING,¹ MATTHEW T. HUMMON,¹  AND CORT JOHNSON²

¹*Time and Frequency Division, National Institute of Standards and Technology, 325 Broadway, Boulder, CO 80305, USA*

²*The Charles Stark Draper Laboratory, Inc., Cambridge, MA 02139, USA*

³*These authors contributed equally to this work*

*zachary.newman@nist.gov

Abstract: Optical frequency standards, or lasers stabilized to atomic or molecular transitions, are widely used in length metrology and laser ranging, provide a backbone for optical communications and lie at the heart of next-generation optical atomic clocks. Here we demonstrate a compact, low-power optical frequency reference based on the Doppler-free, two-photon transition in rubidium-87 at 778 nm implemented on a micro-optics breadboard. Our optical reference achieves a fractional frequency instability of $2.9 \times 10^{-12} / \sqrt{\tau}$ for averaging times τ less than 10^3 s, has a volume of ≈ 35 cm³ and operates on ≈ 450 mW of electrical power. The advanced optical integration presented here demonstrates a key step towards the development of compact optical clocks and the broad dissemination of SI-traceable wavelength references.

© 2020 Optical Society of America under the terms of the [OSA Open Access Publishing Agreement](#)

1. Introduction

Since their development in the mid 1950s, atomic clocks have revolutionized measurement science [1] and fundamental physics [2] and have enabled the development of critical technologies such as the global positioning system. The current generation of compact (<1 L), low-power (<10 W), atomic clocks rely on ground-state, microwave transitions in alkali atoms [3,4]. Although frequency standards based on lasers stabilized to optical transitions are widely recognized as being advantageous for precision timekeeping due to their high quality factors and relative insensitivity to environmental factors [5], broad adoption of optical clocks for field-based timing applications [6,7] has largely been prohibited due to the added complication of counting optical frequencies in a compact device. However, advances in the fields of fiber-based [8,9] and microresonator [10–14] optical frequency combs bring a fully integrated optical clock within reach. Furthermore, compact optical standards could be used to realize SI-traceable references for frequency, wavelength, current and voltage outside the laboratory setting [15,16].

Laboratory-scale optical atomic clocks based on laser-cooled, trapped atoms and ions achieve stabilities at a few parts in 10^{19} [17–20]. These clocks derive their exceptional stability by probing doubly-forbidden, intercombination transitions in atoms with an ultra-stable laser. While such clock transitions offer extremely narrow linewidths (≈ 1 mHz for strontium), accessing these states is experimentally challenging, requiring laser-cooling and trapping in an ultra-high vacuum chamber and prestabilization of the clock laser to a high-finesse optical cavity. Transportable versions of these optical frequency references based on ultra-cold atoms leverage this exquisite sensitivity at the 10^{-18} level for applications in relativistic geodesy and tests of general relativity, but still occupy relatively large volumes (>100 L) and require hundreds of watts to operate [21–23].

Although they have significantly broader linewidths ($\approx 10^5$ to 10^7 Hz), optical transitions in the alkali metals and simple molecules [24–26], such as the rubidium two-photon transition [27], are attractive candidates for compact, low power optical clocks. These transitions can be addressed with commercially-available, narrow-linewidth sources, and Doppler-free interrogation schemes can be employed that eliminate the need for laser cooling and ultra-high vacuum. Additionally, the fast relaxation times of excited atoms enables high-bandwidth feedback to the clock laser, which enables robust operation on moving platforms [26,28]. In fact, several groups have demonstrated vapor cell optical standards [25,28–30] that achieve short-term instabilities competitive with (or outperforming) state-of-the-art, portable microwave clocks [31–33]. An important step for optical clocks to be widely adopted for commercial applications, where microwave clocks presently dominate, is to reduce their size and power and improve manufacturability while maintaining the high stability performance demonstrated by table-top optical frequency references.

Here we introduce a miniaturized (≈ 35 cm³), low-power (≈ 450 mW) optical reference based on millimeter-scale optical components in which a semiconductor laser is stabilized to a microfabricated rubidium vapor cell. Our optical reference achieves a fractional frequency instability of $2.9 \times 10^{-12} / \sqrt{\tau}$, for averaging times τ less than 10^3 s, and we observe a linear drift of 2.1×10^{-13} /h at integration times longer than 10^3 s. This represents a substantial improvement in stability (5 times lower drift rate, 10 to 100 times lower short-term instability) compared with other handheld and battery-operated clocks and optical frequency references [26,34,35]. Furthermore, we emphasize the optical reference uses mostly commercial-off-the-shelf optical components and is assembled using micro-positioning techniques common to commercial laser device assembly.

2. Miniature optical reference

The $5S_{1/2}(F=2) \rightarrow 5D_{5/2}(F=4)$, two-photon transition in rubidium-87 at 778 nm serves as the frequency reference for our laser (described in detail elsewhere [36–39]). Figures 1(a) and (b) show the optical assembly that enables Doppler-free spectroscopy of the rubidium two-photon transition. The individual components that comprise the optical reference are off-the-shelf optics (with the exception of the cell and magnetic shield) that are held in custom-machined aluminum mounts, aligned using a micro-positioning system and set in place on an aluminum baseboard with a UV-curing epoxy.

Figure 1(d) shows a spectrum (blue dots) of two of the hyperfine components ($F=4,3$) of the two-photon transition as the laser frequency is swept across the resonance. We detect excitation of this transition via fluorescence at 420 nm from the $5D \rightarrow 6P \rightarrow 5S$ decay, which is collected with a photomultiplier tube (PMT). A fit (red line) to the spectrum gives a linewidth of 2.2 MHz ($F=4$). While this is substantially broader than the natural linewidth (330 kHz), it is not the limiting factor in the clock frequency stability. An independent measurement with an externally aligned narrow linewidth (40 kHz) laser yields a fluorescence spectrum of similar (1.9 MHz) linewidth, indicating broadening is likely due to residual contaminant background gas.

The optical reference presented here employs an in-line geometry for probing and measuring the two-photon transition [40], in which the counter-propagating beams necessary for avoiding Doppler-broadening of the transition are generated by retro-reflecting the laser off a high reflectivity dielectric coating on the back of a planar, microfabricated cell (described below). Excitation of the transition is detected by collecting fluorescence directly behind the cell rather than from the side of the cell as is typically done in laboratory scale rubidium two-photon standards [37–39]. This in-line detection allows us to place the PMT close to the cell, resulting in a compact geometry with good collection efficiency.

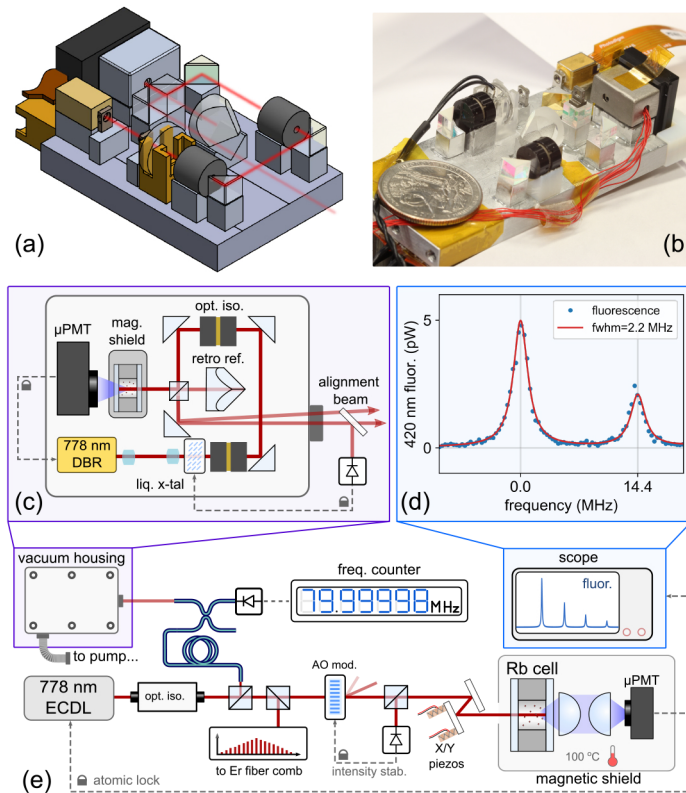


Fig. 1. Schematic (a) and image (b) of the miniature optical reference. The optical reference consists of a 778 nm distributed-Bragg-reflector (DBR) laser, a series of miniature optical elements, an atom source (microfabricated vapor cell and shield) and a microfabricated photomultiplier tube (PMT). (c) Overhead schematic of the miniature physics package. The laser path is indicated by red arrows similar to (a). (d) Spectrum of the $5S_{1/2} \rightarrow 5D_{5/2}$ two-photon transition in rubidium-87. (e) Optical layout of the measurement system.

2.1. Description of the optical reference

In order to orient the reader, we briefly describe the operation of the optical reference by detailing the optical path of the laser that is traced out by a red arrow in Figs. 1(a) and (c). Light emitted from the DBR laser, which diverges sharply, is shaped with a telescope consisting of $f = 1.45$ mm and 5 mm lenses. The lenses are arranged such that the laser is nominally focused at the back of the vapor cell with horizontal and vertical beam waists of ≈ 200 μm and ≈ 100 μm , respectively. For this beam waist, the light shift was measured to be ≈ 4.19 kHz/mW.

Immediately following the telescope, the beam passes through a variable attenuator used for intensity stabilization comprised of a half waveplate, liquid crystal retarder, and a miniature optical isolator. The beam then passes through a pair of turning mirrors and through a second isolator to further reduce optical feedback to the laser. The isolators are positioned ≈ 2 cm apart so their individual magnetic fields do not interfere with each other and as far away from the vapor cell as possible (while maintaining a compact footprint). Following a third mirror, a 90/10, non-polarizing beam splitter directs ninety percent of the light into the vapor cell and passes the remaining ten percent onto a fourth mirror, which directs it away from the cell to serve as the ‘output beam’. The output beam is used to characterize the laser frequency, monitor and stabilize the laser intensity and for alignment purposes.

Light entering the cell is reflected back towards the beam splitter by a high-reflectivity optical coating on the rear window of the cell. A fraction of this light passes through the beam splitter, is retro-reflected from a corner cube and ultimately follows the same path as the output beam (labeled the 'alignment beam' in Fig. 1(c)). During construction, the forward and backward propagating beams that drive the two-photon transition are aligned by overlapping the output beam and the retro-reflected beam by adjusting the angle and position of the cell before it is epoxied in place. After assembly, the alignment beam to the corner cube is blocked.

2.2. Optical alignment

Figure 2 shows a set of images of the micropositioning system used to populate the optical reference. The most critical alignments are the positions of the two lenses that comprise the telescope at the output of the laser and the angular alignment of the beam splitter (Fig. 1(c)). Precision alignment of these components is achieved using a six-degree-of-freedom, hexapod micropositioning system (ALIO Industries AI-HEX-HR2-SS). The hexapod consists of a platform mounted atop six piezo-actuated legs, each of which has optically-encoded feedback that enables position resolution of 20 nm and an effective angular resolution of 1 μ rad. During assembly, precision placement of these components is achieved by mechanically connecting them to the platform, moving the platform relative to the immobile aluminum baseplate, and securing them to the baseplate using a low-shrinkage, UV-cure epoxy (Dymax OP-4-20632). During the curing stage, we monitor the laser position and focus to ensure alignment is maintained as the epoxy cures. Figure 1(c) illustrates the procedure for aligning the interrogation beams.

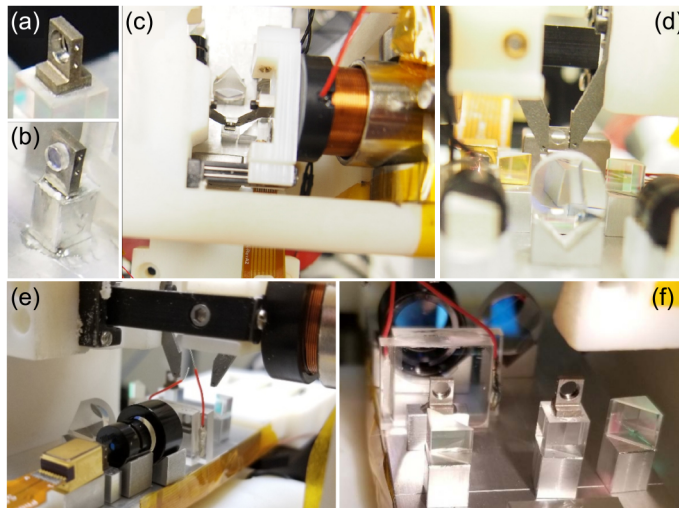


Fig. 2. Micro-optics breadboard assembly: (a) and (b) show a beam splitter and a lens epoxied to a custom mount that facilitates precision alignment during assembly of the miniaturized optical frequency reference. (c) and (d) show the custom mount securely captured by a set of steel jaws. The jaws are mechanically connected to a hexapod micropositioning platform, enabling precision alignment of the optic while it is secured to the aluminum baseplate with UV cure epoxy. (e) and (f) show alternate views of the micropositioning system during assembly of an earlier version of the optical reference.

The platform-to-optic mechanical interface is facilitated by epoxying each optical component to a custom optical mount as shown in 2(a) and (b). The mount is then captured by a set of custom steel jaws, which are shown from two different angles during assembly of the frequency reference in Figs. 2(c) and (d). The mount and the jaws have mating features to ensure a robust

and repeatable mechanical connection. The jaws are actuated via a voice coil actuator visible on the right side of Fig. 2(c) and controlled with an external voltage. The control level is set to apply sufficient but minimal force when curing to avoid adding strain that could misalign the optic upon releasing the mount from the jaws.

2.3. Atom source

The vapor cell, shown in Fig. 3(b) is assembled by anodically bonding two pieces of glass to a silicon frame under vacuum [41,42]. The front window is uncoated borosilicate glass and the back window is an aluminosilicate window with a high-reflectivity coating. Before bonding, the cell is filled in a nitrogen-purged glovebox by dipping a gold-coated copper wire in liquid rubidium metal and placing the wire inside the cell. A non-evaporable getter is also placed in the cell before bonding and is laser activated after bonding [43].

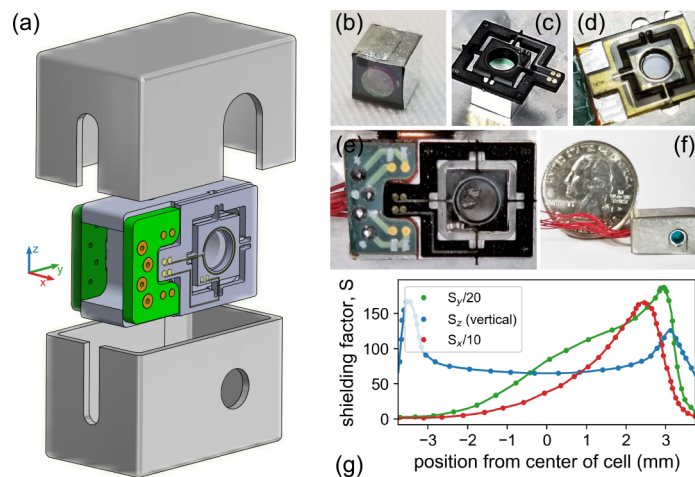


Fig. 3. (a) Schematic of atom source assembly, showing the magnetic shield, the aluminum cell mount and thermal tethers. Photographs taken during the assembly of the atom source showing the: (b) vapor cell, (c) thermal tethers, (d) aluminum mount (e) heater electronic connections (f) fully assembled source inside magnetic shield. (g) Simulated shielding factor from the center of the cell due to the optical isolators.

Figure 3 gives a detailed view of the atom source, which consists of a microfabricated vapor cell held on an aluminum mount. This mount is epoxied into the bottom half of a custom, single-layer magnetic shield. Figure 3(g) shows a finite element simulation of the shielding factor at the center of the vapor cell in the presence of the magnetic field from the two optical isolators. Magnetic field attenuation is weakest in the vertical (z) direction where there is a single layer of shielding. Even still, the shielding factor in this direction is ≈ 60 and is sufficient to prevent spectral broadening from the isolators. A second shield surrounding the entire device would further reduce magnetic sensitivity. The cell is thermally isolated from the mount by a pair of laser-cut, polyimide tethers that suspend the cell in the middle of the aluminum frame, and it is heated by a pair of integrated platinum heater traces deposited on the tethers. The tethers and heaters are visible in Figs. 3(c) and (d). In order to avoid convective heat loss and reduce the total power consumption, the entire optical breadboard was housed in a small vacuum chamber (see Fig. 1(e)). During measurements we operate the vacuum chamber near 10^{-7} Torr, although pressures below 10^{-4} Torr are sufficient to reduce thermal losses. The cell can reach a temperature of ≈ 100 °C using only 44 mW of electrical power when heated under vacuum.

Tests measuring the power draw versus cell temperature were performed on five cells suspended in an aluminum mount by a pair of Cirlex polyimide suspensions. Suspensions are used to thermally isolate the cell from the aluminum mount through four narrow tethers of varying length and width (see Fig. 3). The power required to heat the cell to a given temperature then depends on the conductive loss through the tethers as well as radiative loss to the surrounding environment. The heaters were tested in sub-millitorr vacuum, where convective losses were negligible. The results of this measurement are shown in Fig. 4.

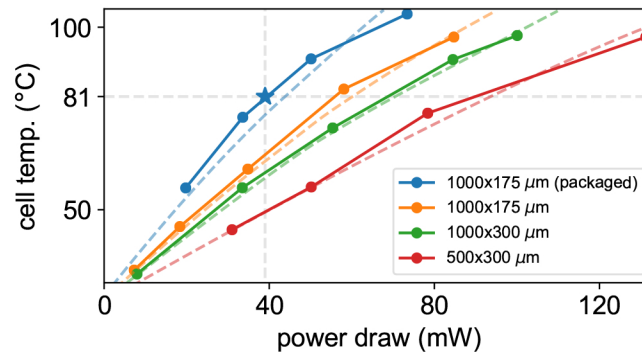


Fig. 4. Power draw versus cell temperature for a set of four polyimide suspensions with various tether geometries. Tethers are labeled by their length and width. All tethers are 500 μm thick. The data point marked with a star denotes the tether and power value used for the optical reference.

Dashed curves in the figure show the modeled radiative and conductive losses, which are given by

$$P_{\text{cell}} = \epsilon\sigma A (T^4 - T_0^4) + 8k \frac{wt}{l} (T - T_0) \quad (1)$$

where ϵ is the characteristic emissivity of the cell/suspension, σ is the Stefan-Boltzmann constant, A is the surface area of the cell, T is the cell temperature, T_0 is the temperature of the surrounding environment, k is the thermal conductivity (0.17 W/mK for Cirlex), and l , w , and t are the length, width and thickness of the individual tethers. The first term of the model accounts for the radiative loss. The second term accounts for the combined conductive loss through the eight tethers of the two suspensions. Four of the devices tested were mounted in an open test fixture with no enclosure. The final test was performed on the packaged device (blue), encased in a magnetic shield that reduces radiative losses.

To estimate the relative contribution to the total loss of the radiative and conductive subcomponents, we simultaneously fit the above model to the results of all four devices in the test fixture, leaving only the emissivity and the tether thermal conductivity as free parameters. The fit results indicate that heat loss in the narrowest and longest tethers (1000 μm×175 μm) is dominated by

Table 1. Power budget for miniature physics package

Component	Power draw (mW)
cell heater (81 °C)	39
clock laser (147 mA)	294
liquid x-tal mod.	11
μ-PMT	90
Total power draw	434

radiation: at 100 °C, approximately 80% (69 mW) of the total loss is via radiation. In contrast, the loss is evenly split between conduction and radiation for the shortest and widest tethers (500 μm \times 300 μm). For the packaged device, 100 °C, the radiative loss is reduced by one-third compared to the open test fixture (44 mW versus 69 mW).

Table 1 shows the measured total power draw of the physics package broken down by component.

3. Frequency instability and temperature sensitivity

We measure the laser frequency by beating a portion of the output light against an external cavity diode laser (ECDL) locked to a second rubidium two-photon optical reference (Fig. 1(e)). The frequency of the ECDL was shifted by 80 MHz using an acousto-optical modulator and locked to the same hyperfine transition as the miniature optical reference. We detect the 80 MHz beat using a standard silicon photodiode. The frequency instability of the ECDL was measured against a self-referenced, erbium-fiber frequency comb stabilized to a high finesse optical cavity and was found to be below $5 \times 10^{-13} / \sqrt{\tau}$, where τ is the averaging time in seconds, and does not limit our measurements of the miniature optical reference.

Figure 5(a) gives measurements of the laser frequency over a period of 15 h for cell temperatures of 81.5 °C (blue) and 99 °C (green), which shows a clear temperature-dependent, linear drift. In both cases, the optical power seen by the atoms during the measurements was ≈ 15.1 mW (Fig. 6(d), dark orange). Figure 5(b) gives the corresponding Allan deviation when the cell is operated at 81.5 °C and 99 °C, respectively. To achieve the lowest short-term instability, optical references using this two-photon transition typically operate the cell temperature near 100 °C to increase the rubidium vapor pressure and achieve high signal-to-noise ratio [39,40]. However, in our case, the short-term instability of the miniature optical reference is limited by intermodulation noise [44] on the DBR laser of $\approx 3 \times 10^5$ Hz²/Hz, corresponding to an instability limit of $\approx 1.4 \times 10^{-12} / \sqrt{\tau}$. Thus we choose to operate the miniature optical reference near 80 °C to reduce long-term drift without sacrificing short-term instability and robust locking.

The long-term frequency drift is the dominant systematic effect and prevents a meaningful characterization of the accuracy of our optical reference. However, in prior work from our group [40], we measured the uncertainty of a similar optical standard comprised of unintegrated, microfabricated components to be $\approx 2 \times 10^{-11}$. The measurements in the remainder of the paper attempt to identify the source of and characterize the drift with the goal of eliminating this effect in future implementations.

Figure 6 shows a set of measurements designed to assess the temperature sensitivity of the optical reference where we repeatedly dropped the cell temperature to 40 °C by reducing the cell heater current. During the measurements we monitored the laser frequency along with other system parameters including the in-loop laser power, cell heater voltage, and the fluorescence level (Fig. 6(d)). Figure 6(a) shows the laser frequency over the course of the measurement where the breaks in the data correspond to periods where the cell temperature was 40 °C (we cannot operate the optical reference at low temperatures since the fluorescence signal used to lock the laser is too weak to engage the lock).

For the three periods where the cell temperature has stabilized at 80 °C, denoted in blue, the drift rates are comparable: $\approx 3.4 \times 10^{-13}$ /h, $\approx 2.6 \times 10^{-13}$ /h, and $\approx 2.9 \times 10^{-13}$ /h. The inset gives a plot of the laser frequency for $T_{\text{cell}} = 80$ °C as a function of the corrected time, i.e. we remove time periods where the cell temperature is at 40 °C. We note that in this corrected timescale, the laser frequency fits to a single linear drift rate, indicating that the mechanism that causes the drift does not continue to evolve when the cell is cold. We use this corrected timescale to determine a linear drift rate at 80 °C for the full measurement.

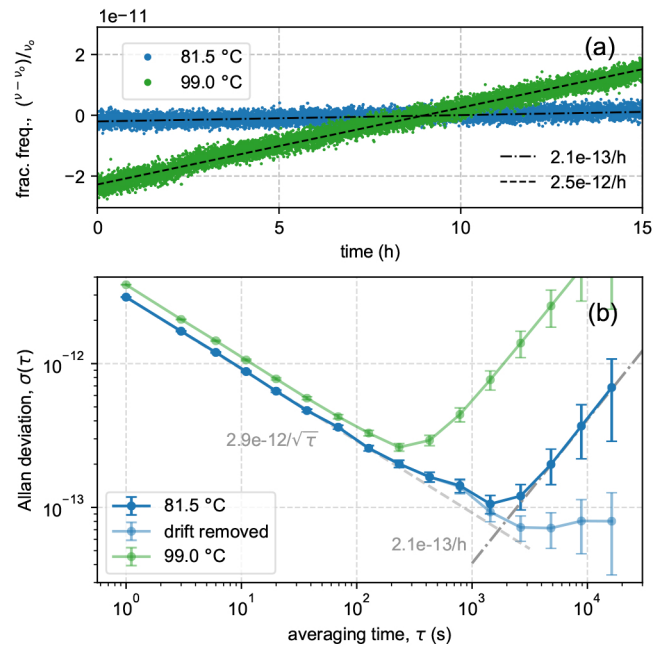


Fig. 5. Frequency instability of the miniature optical reference. (a) Time series of the optical reference taken with the cell temperature at 81.5 °C (blue) and 99 °C (green) during two different 15 hr time windows. Dashed lines indicate fitted drift rates. (b) Allan deviation of the optical reference at 81.5 °C and 99 °C, respectively. Error bars represent 68% confidence interval.

To investigate the instability of the optical reference beyond its drift limited performance we analyze two cases. First, Fig. 5(b) shows the time series with the drift removed has an instability flicker noise floor of 1×10^{-13} for 10^3 s to 10^4 s, comparable to that observed in [40], which used similar optical components in a table top assembly. Second, Fig. 6(b) shows the laser frequency with the drift rate, $f(t)$, removed. The dotted lines show the average frequency (color coded) for each of the three periods where $T_{\text{cell}} = 80$ °C. The frequency difference between consecutive measurements (Δy_x) is noted above the data, with agreement at the several 10^{-13} level. This suggests that long-term stability at the 10^{-13} level may be possible with this type of optical reference with further improvements to reduce the drift.

Figure 6(d) gives a plot of the fluorescence (dark blue) which decays as the measurement progresses. We have considered a number of potential physical effects that could lead to a frequency shift and corresponding change in fluorescence including light shifts, the depletion of rubidium in the cell, evolution of background gases, migration of liquid-phase rubidium across the cell windows and the diffusion of helium through the cell windows. We conservatively estimate the frequency shift due to the Rb-Rb collision shift [39] from changes in cell temperature to be less than 10^{-13} (or 40 Hz). Ultimately we suspect the frequency drift is associated with misalignment of the interrogation beams at elevated temperatures as the epoxy securing the optical elements approaches its glass transition temperature. Changes in the baseplate temperature, measured indirectly via the cell heater voltage (Fig. 6(c), pink) support this hypothesis.

As discussed in Martin *et al.* [45], imperfect alignment of the interrogation beams in a two-photon transition can lead to a frequency shift (via the ac-Stark effect) since atoms in different parts of the cell experience different optical intensities. As a result, unstable optical alignment can lead to frequency instabilities in the clock laser. To characterize this shift (Fig. 7), we use

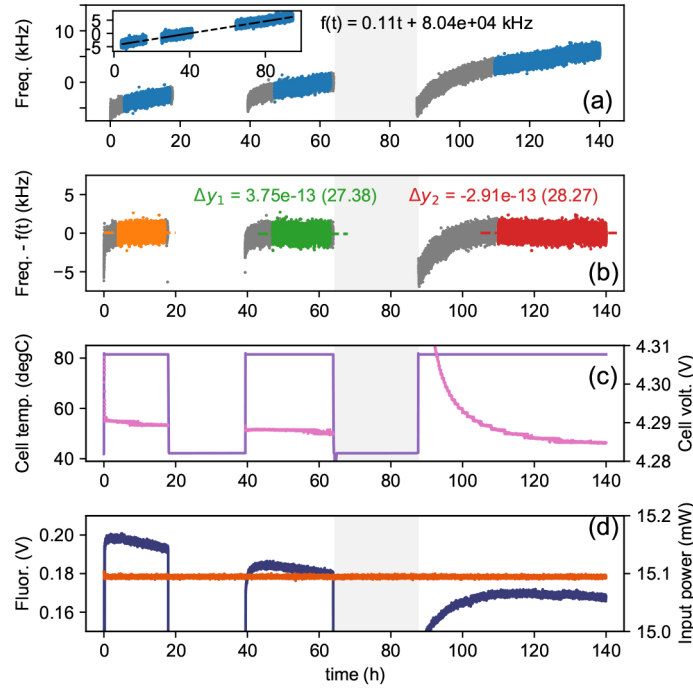


Fig. 6. Measurement of the clock laser frequency along with other system parameters over 140 h. (a) Laser frequency during the measurement (grey) and the period where the frequency drifts linearly (blue). The inset shows the laser frequency only during the periods where $T_{\text{cell}} = 80^\circ\text{C}$ and the frequency drifts linearly. (b) Laser frequency with the drift rate calculated in the inset removed. (c) Cell temperature and cell heater voltage. (d) Fluorescence level and in-loop input power. During the period between 65 and 85 h (shaded light gray) the vacuum box was vented in order to test frequency shifts due to changes in the cell atmosphere.

the auxiliary optical reference described at the beginning of Sec. 3 where we have direct access to the alignment of the interrogation beams. Initially the interrogation beams are aligned by hand to maximize fluorescence ($\theta = 0$). From there, we use piezo actuators on the mirror closest to the cell to adjust the input beam angle with respect to $\theta = 0$. We then measure the beam displacement (and the corresponding deflection angle) of the reflected beam using a quadrant photodetector (Fig. 7(a)). Figure 7(b) shows a plot of the clock frequency shift and the normalized fluorescence level as a function of the misalignment angle, which depends quadratically on the angle. Interestingly, there is a slight offset in alignment angle corresponding to the local minimum in frequency shift compared to that of the fluorescence.

While we do not have a way of measuring the misalignment shift of the miniature optical reference directly, the auxiliary optical reference should serve as a reasonable proxy as the two optical references operate under similar conditions: both optical standards use a microfabricated vapor cell, the same photomultiplier tube to detect fluorescence and the beam waist and intensity of the interrogation beams are within a factor of two.

Figure 7(c) shows a plot of the laser frequency and normalized fluorescence for the miniature optical reference (similar to Fig. 6(d)). Over the course of the 80 h measurement, the fluorescence signal decreases by $\approx 40\%$, while the frequency drifts by ≈ 10 kHz. We observe a similar change in frequency of the auxiliary optical reference in response to a misalignment of the

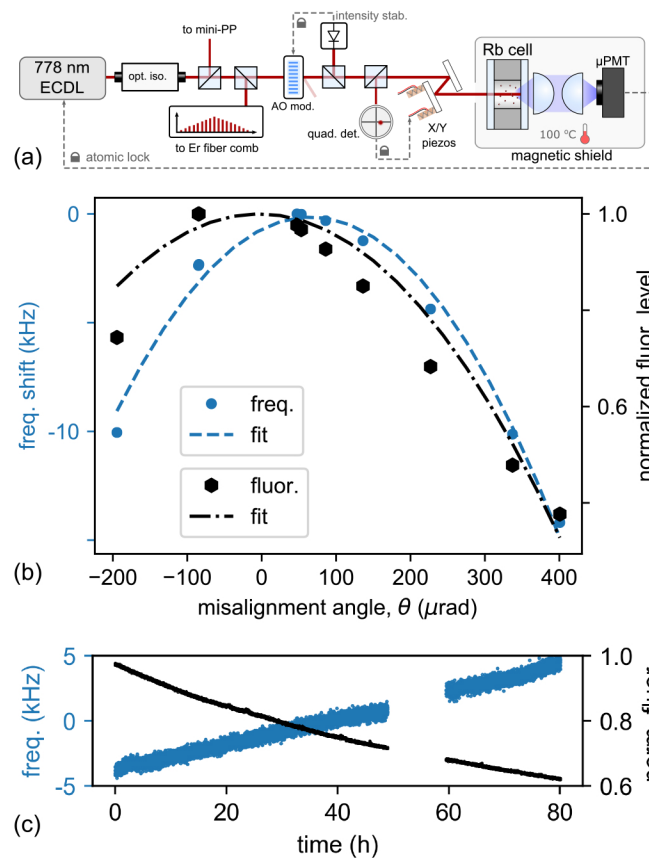


Fig. 7. (a) Schematic of setup for testing misalignment shift. The critical components used to evaluate this shift are the piezo actuated mirror immediately before the cell and a quadrant detector which registers the position of the reflected beam (in X and Y respectively) via the sum of the photocurrents in each direction. (b) Frequency shift (blue) and fluorescence signal (black) as a function of misalignment angle in the two directions measured by stepping the voltage on the piezo mirror while the clock is running. (c) Frequency drift (blue) and the corresponding decay in 420 nm fluorescence (black) over a three day period for the miniature optical reference.

interrogation beams. We suspect optical misalignment is caused by thermal gradients on the aluminum baseplate that results in temperature dependent strain on the epoxy holding the optical components in place.

4. Conclusion

The advanced optical integration presented here demonstrates the feasibility of high-performance, compact, atomic clocks and wavelength references based on Doppler-free, optical transitions in warm atomic vapors. Even with the observed drift, the laser frequency instability is an order of magnitude better than commercially available microwave clocks of similar size at a fraction of the operating power [46]. To minimize drift rates, devices employing ultra-stable [47] or microfabricated [48] optical assemblies are needed. With further engineering, it is reasonable to expect that misalignment of the interrogation beams could be suppressed, resulting in significantly improved long-term frequency instability.

Funding

Defense Advanced Research Projects Agency; Atomic Clocks with Enhanced Stability.

Acknowledgements

The authors would like to thank Tara Fortier for help with frequency measurements of the reference laser and Jordan Stone and Liron Stern for comments on the manuscript. The views, opinions and/or findings expressed are those of the authors and should not be interpreted as representing the official views or policies of the Department of Defense or the U.S. Government. Any mention of commercial products within NIST web pages is for information only; it does not imply recommendation or endorsement by NIST. Distribution Statement "A" (Approved for Public Release, Distribution Unlimited).

Disclosures

The authors declare no conflicts of interest.

References

1. K. M. Evenson, J. S. Wells, F. R. Petersen, B. L. Danielson, G. W. Day, R. L. Barger, and J. L. Hall, "Speed of light from direct frequency and wavelength measurements of the methane-stabilized laser," *Phys. Rev. Lett.* **29**(19), 1346–1349 (1972).
2. J. Hafele and R. E. Keating, "Around-the-World Atomic Clocks: Predicted Relativistic Time Gains," *Science* **177**(4044), 166–168 (1972).
3. S. Knappe, V. Shah, P. D. Schwindt, L. Hollberg, J. Kitching, L. A. Liew, and J. Moreland, "A microfabricated atomic clock," *Appl. Phys. Lett.* **85**(9), 1460–1462 (2004).
4. R. Lutwak, "The Sa.45S Chip-Scale Atomic Clock - Early Production Statistics," *Proceedings of the 43rd Annual Precise Time and Time Interval Systems and Applications Meeting*, pp. 207–220 (2011).
5. P. Gill, "Optical frequency standards," *Metrologia* **42**(3), S125–S137 (2005).
6. C. Clivati, G. A. Costanzo, M. Frittelli, F. Levi, A. Mura, M. Zucco, R. Ambrosini, C. Bortolotti, F. Perini, M. Roma, and D. Calonico, "A coherent fiber link for very long baseline interferometry," *IEEE Trans. Sonics Ultrason.* **62**(11), 1907–1912 (2015).
7. J. Vig, "Military applications of high accuracy frequency standards and clocks," *IEEE Trans. Sonics Ultrason.* **40**(5), 522–527 (1993).
8. P. Manurkar, E. F. Perez, D. D. Hickstein, D. R. Carlson, J. Chiles, D. A. Westly, E. Baumann, S. A. Diddams, N. R. Newbury, K. Srinivasan, S. B. Papp, and I. Coddington, "Fully self-referenced frequency comb consuming 5 watts of electrical power," *OSA Continuum* **1**(1), 274 (2018).
9. L. C. Sinclair, I. Coddington, W. C. Swann, G. B. Rieker, A. Hati, K. Iwakuni, and N. R. Newbury, "Operation of an optically coherent frequency comb outside the metrology lab," *Opt. Express* **22**(6), 6996 (2014).
10. M. H. P. Pfeiffer, C. Herkommer, J. Liu, H. Guo, M. Karpov, E. Lucas, M. Zervas, and T. J. Kippenberg, "Octave-spanning dissipative Kerr soliton frequency combs in Si₃N₄ microresonators," *Optica* **4**(7), 684–690 (2017).

11. T. C. Briles, J. R. Stone, T. E. Drake, D. T. Spencer, C. Frederick, Q. Li, D. A. Westly, B. R. Illic, K. Srinivasan, S. A. Diddams, and S. B. Papp, "Interlocking Kerr-microresonator frequency combs for microwave to optical synthesis," *Opt. Lett.* **43**(12), 2933–2936 (2018).
12. A. S. Raja, J. Liu, N. Volet, R. N. Wang, J. He, E. Lucas, R. Bouchand, P. Morton, J. Bowers, and T. J. Kippenberg, "Packaged photonic chip-based soliton microcomb using an ultralow-noise laser," arXiv, pp. 3–7 (2019).
13. B. Stern, X. Ji, Y. Okawachi, A. L. Gaeta, and M. Lipson, "Battery-operated integrated frequency comb generator," *Nature* **562**(7727), 401–405 (2018).
14. M.-G. Suh, C. Y. Wang, C. Johnson, and K. Vahala, "Directly pumped 10 GHz microcomb modules from low-power diode lasers," *Opt. Lett.* **44**(7), 1841–1843 (2019).
15. BIPM rubidium 778-nm transition recommended values, https://www.bipm.org/utls/common/pdf/mep/M-e-P_Rb_778.pdf.
16. J. Kitching, E. A. Donley, S. Knappe, M. Hummon, A. T. Dellis, J. Sherman, K. Srinivasan, V. A. Aksyuk, Q. Li, D. Westly, B. Roxworthy, and A. Lal, "NIST on a Chip: Realizing SI units with microfabricated alkali vapour cells," *J. Phys.: Conf. Ser.* **723**, 012056 (2016).
17. W. F. McGrew, X. Zhang, H. Leopardi, R. J. Fasano, D. Nicolodi, K. Beloy, J. Yao, J. A. Sherman, S. A. Schäffer, J. Savory, R. C. Brown, S. Römisch, C. W. Oates, T. E. Parker, T. M. Fortier, and A. D. Ludlow, "Towards Adoption of an Optical Second: Verifying Optical Clocks at the SI Limit," *Optica* **6**(4), 448–454 (2019).
18. S. M. Brewer, J. Chen, A. M. Hankin, E. R. Clements, C. W. Chou, D. J. Wineland, D. B. Hume, and D. R. Leibbrandt, "An 27-Al⁺ quantum-logic clock with systematic uncertainty below 10⁻¹⁸," arXiv, pp. 1–5 (2019).
19. T. Bothwell, D. Kedar, E. Oelker, J. M. Robinson, S. L. Bromley, W. L. Tew, J. Ye, and C. J. Kennedy, "JILA SrI optical lattice clock with uncertainty of," *Metrologia* **56**(6), 065004 (2019).
20. E. Oelker, R. B. Hutson, C. J. Kennedy, L. Sonderhouse, T. Bothwell, A. Goban, D. Kedar, C. Sanner, J. M. Robinson, G. E. Marti, T. Legero, M. Giunta, R. Holzwarth, F. Riehle, U. Sterr, and J. Ye, "Demonstration of 4.8x10⁻¹⁷ stability at 1s for two independent optical clocks," *Nat. Photonics* **13**(10), 714–719 (2019).
21. J. Grotti, S. Koller, S. Vogt, S. Häfner, U. Sterr, C. Lisdat, H. Denker, C. Voigt, L. Timmen, A. Rolland, F. N. Baynes, H. S. Margolis, M. Zampaolo, P. Thoumany, M. Pizzocaro, B. Rauf, F. Bregolin, A. Tampellini, P. Barbieri, M. Zucco, G. A. Costanzo, C. Clivati, F. Levi, and D. Calonico, "Geodesy and metrology with a transportable optical clock," *Nat. Phys.* **14**(5), 437–441 (2018).
22. S. Origlia, M. S. Pramod, S. Schiller, Y. Singh, K. Bongs, R. Schwarz, A. Al-Masoudi, S. Dörscher, S. Herbers, S. Häfner, U. Sterr, and C. Lisdat, "Towards an optical clock for space: Compact, high-performance optical lattice clock based on bosonic atoms," *Phys. Rev. A* **98**(5), 053443 (2018).
23. M. Takamoto, I. Ushijima, N. Ohmae, T. Yahagi, K. Kokado, H. Shinkai, and H. Katori, "Test of general relativity by a pair of transportable optical lattice clocks," *Nat. Photonics* **14**(7), 411–415 (2020).
24. J. L. Hall, L.-S. Ma, M. Taubman, B. Tiemann, F.-I. Hong, O. Pfister, and J. Ye, "Stabilization and Frequency Measurement of the I2-Stabilized Nd:YAG Laser," *IEEE Trans. Instrum. Meas.* **48**(2), 583–586 (1999).
25. T. Schuldt, K. Döringshoff, E. V. Kovalchuk, A. Keetman, J. Pahl, A. Peters, and C. Braxmaier, "Development of a compact optical absolute frequency reference for space with 10-15 instability," *Appl. Opt.* **56**(4), 1101–1106 (2017).
26. M. Lezius, T. Wilken, C. Deutsch, M. Giunta, O. Mandel, A. Thaller, V. Schkolnik, M. Schiemangk, A. Dinkelaker, A. Kohfeldt, A. Wicht, M. Krutzik, A. Peters, O. Hellmig, H. Duncker, K. Sengstock, P. Windpassinger, K. Lampmann, T. Hülasing, T. W. Hänsch, and R. Holzwarth, "Space-borne frequency comb metrology," *Optica* **3**(12), 1381 (2016).
27. G. Grynberg and B. Cagnac, "Doppler-free multiphotonic spectroscopy," *Rep. Prog. Phys.* **40**(7), 791–841 (1977).
28. K. Döringshoff, F. B. Gutsch, V. Schkolnik, C. Kürbis, M. Oswald, B. Pröbster, E. V. Kovalchuk, A. Bawamia, R. Smol, T. Schuldt, M. Lezius, R. Holzwarth, A. Wicht, C. Braxmaier, M. Krutzik, and A. Peters, "Iodine Frequency Reference on a Sounding Rocket," *Phys. Rev. Appl.* **11**(5), 054068 (2019).
29. J. Ye, L. S. Ma, and J. L. Hall, "Molecular Iodine Clock," *Phys. Rev. Lett.* **87**(27), 270801 (2001).
30. E. J. Zang, J. P. Cao, Y. Li, C. Y. Li, Y. K. Deng, and C. Q. Gao, "Realization of Four-Pass I2 Absorption Cell in 532-nm Optical Frequency Standard," *IEEE Trans. Instrum. Meas.* **56**(2), 673–676 (2007).
31. F. X. Esnault, N. Rossetto, D. Holleville, J. Delporte, and N. Dimarcq, "HORACE: A compact cold atom clock for Galileo," *Adv. Space Res.* **47**(5), 854–858 (2011).
32. J. Savory, A. Banducci, S. R. Jefferts, F. Ascarrunz, Y. Dudin, M. Delgado Aramburo, and L. Azcarrunz, "A Portable Cold 87-Rb Atomic Clock with Frequency Instability at One Day in the 10-15 Range," *2018 IEEE International Frequency Control Symposium (IFCS)*, 1–3 (2018).
33. AOSense Cold-atom frequency standard data sheet, <https://aosense.com/wp-content/uploads/2018/02/Cold-Atom-Frequency-Standard.pdf>.
34. J. Pohl, D. Feise, A. Sahm, P. Leisching, G. Blume, D. Jedrzejczyk, K. Paschke, and C. Nölleke, "Frequency locking of compact laser-diode modules at 633 nm," in *Photonic Instrumentation Engineering V*, vol. 10539 Y. G. Soskind, ed. (SPIE-Intl Soc Optical Eng, 2018), p. 6.
35. J. Kitching, "Chip-scale atomic devices," *Appl. Phys. Rev.* **5**(3), 031302 (2018).
36. L. Hilico, R. Felder, D. Touahri, O. Acef, A. Clairon, and F. Biraben, "Metrological features of the rubidium two-photon standards of the BNM-LPTF and Kastler Brossel Laboratories," *Eur. Phys. J.: Appl. Phys.* **4**(2), 219–225 (1998).
37. M. Poulin, C. Latrasse, D. Touahri, and M. Têtu, "Frequency stability of an optical frequency standard at 192.6 THz based on a two-photon transition of rubidium atoms," *Opt. Commun.* **207**(1-6), 233–242 (2002).

38. J. E. Bernard, A. A. Madej, K. J. Siemsen, L. Marmet, C. Latrasse, D. Touahri, M. Poulin, M. Allard, and M. Tetu, "Absolute frequency measurement of a laser at 1556 nm locked to the $5S_{1/2}$ - $5D_{5/2}$ two-photon transition in 87-Rb," *Opt. Commun.* **173**(1-6), 357–364 (2000).
39. K. W. Martin, G. Phelps, N. D. Lemke, M. S. Bigelow, B. Stuhl, M. Wojcik, M. Holt, I. Coddington, M. W. Bishop, and J. H. Burke, "Compact Optical Atomic Clock Based on a Two-Photon Transition in Rubidium," *Phys. Rev. Appl.* **9**(1), 014019 (2018).
40. Z. L. Newman, V. Maurice, T. E. Drake, J. R. Stone, T. C. Briles, D. T. Spencer, C. Fredrick, Q. Li, D. A. Westly, B. R. Illic, B. Shen, M.-G. Suh, K. Youl Yang, C. Johnson, D. M. S. Johnson, L. W. Hollberg, K. J. Vahala, K. Srinivasan, S. A. Diddams, J. E. Kitching, S. B. Papp, and M. T. Hummon, "Architecture for the photonic integration of an optical atomic clock," *Optica* **6**(5), 680–685 (2019).
41. L. A. Liew, S. Knappe, J. Moreland, H. Robinson, L. Hollberg, and J. Kitching, "Microfabricated alkali atom vapor cells," *Appl. Phys. Lett.* **84**(14), 2694–2696 (2004).
42. S. Knappe, V. Gerginov, P. D. D. Schwindt, V. Shah, H. G. Robinson, L. Hollberg, and J. Kitching, "Atomic vapor cells for chip-scale atomic clocks with improved long-term frequency stability," *Opt. Lett.* **30**(18), 2351–2353 (2005).
43. D. R. Scherer, D. B. Fenner, and J. M. Hensley, "Characterization of alkali metal dispensers and non-evaporable getter pumps in ultrahigh vacuum systems for cold atomic sensors," *J. Vac. Sci. Technol., A* **30**(6), 061602 (2012).
44. C. Audoin, V. Candelier, and N. Dimarcq, "A limit to the frequency stability of passive frequency standards due to an intermodulation effect," *IEEE Trans. Instrum. Meas.* **40**(2), 121–125 (1991).
45. K. W. Martin, B. Stuhl, J. Eugenio, M. S. Safronova, G. Phelps, J. H. Burke, and N. D. Lemke, "Frequency Shifts due to Stark Effects on a Rb two-photon transition," *arXiv*, 1–12 (2019).
46. Microsemi Miniature Atomic Clock data sheet.
47. C. J. Killow, E. D. Fitzsimons, J. Hough, M. Perreux-Lloyd, D. I. Robertson, S. Rowan, and H. Ward, "Construction of rugged, ultrastable optical assemblies with optical component alignment at the few microradian level," *Appl. Opt.* **52**(2), 177–181 (2013).
48. M. T. Hummon, S. Kang, D. G. Bopp, Q. Li, D. A. Westly, S. Kim, C. Fredrick, S. A. Diddams, K. Srinivasan, V. Aksyuk, and J. E. Kitching, "Photonic chip for laser stabilization to an atomic vapor with 10-11 instability," *Optica* **5**(4), 443–449 (2018).